

Results of the Inflatable Robotic Rover Testbed

Dimitrios Apostolopoulos, Michael D. Wagner, Stuart Heys
and James Teza

CMU-RI-TR-03-18 ₂

Results of the Inflatable Robotic Rover Testbed

CMU-RI-TR-03-18

Dimitrios Apostolopoulos, Michael D. Wagner, Stuart Heys
and James Teza

Robotics Institute
Carnegie Mellon University
5000 Forbes Avenue
Pittsburgh, PA 15213
June 2003

© 2003 Carnegie Mellon University

Abstract

Inflatable robotic rovers (IRRs) are a promising concept for long-range exploration and access to high-risk areas on planetary surfaces. Through inflation or expansion of their locomotion elements, inflatable rovers can achieve extraordinary terrainability not possible by other conventional mobility systems while maintaining respectable travel speeds. Early work by NASA's Jet Propulsion Laboratory has identified key mobility advantages, but design optimality and limitations relative to mission requirements are currently not known. This paper describes CMU's experimental studies that characterize single robotic wheel performance in terms of rolling resistance, drawbar pull, drive torque, drive power and tire wear. These studies were performed with a testbed apparatus that allowed variation of tire design, wheel speed / acceleration, tire pressure, soil / obstacle properties and traverse length.

Email: da1v@ri.cmu.edu, Tel: 412-268-7224

1 Overview

Inflatable robotic rovers (IRR) are a promising concept for long-range exploration and access to high-risk areas on planetary surfaces. Through inflation or expansion of their locomotion elements, inflatable rovers can achieve extraordinary terrainability not possible by other conventional mobility systems while maintaining respectable travel speeds. Inflatable rovers such as JPL's prototype shown in Figure 1 can drive over extreme terrain and surmount obstacles with ease. This is a distinct advantage over fixed wheel size configurations, which are forced to drive around obstacles. The effect of large diameter inflatable wheels on the performance of a rover is paramount. For example, a rover with drive wheels 1.5 m in diameter would theoretically surmount 90% of discrete obstacles on the Martian surface. Because of low stowage requirements, inflatable rovers offer an advantageous solution for maximizing space rover performance while satisfying fixed mass and volume constraints.

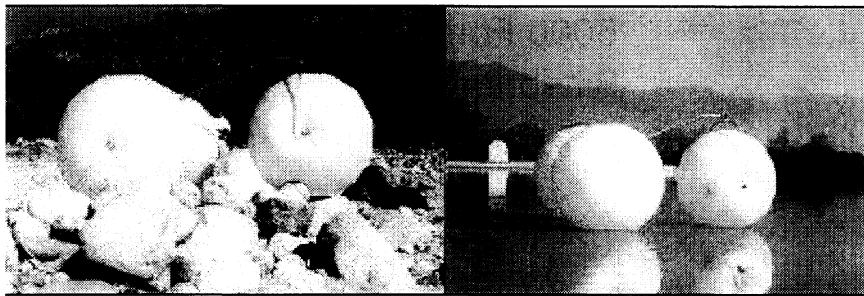


Figure 1: JPL's inflatable rover prototype undergoing field testing. (Courtesy: JPL)

Relevant research is summarized in:

http://www.jpl.nasa.gov/adv_tech/rovers/summary_overview.htm
http://prl.jpl.nasa.gov/projects/inflatable/inflatable_index.html.

These programs seek to elevate inflatable rover technology to a sufficiently high Technology Readiness Level to present a feasible choice for Mars exploration missions in the 2007-09 timeframe. JPL's early work has identified key mobility advantages (robustness to large obstacles, low mass relative to scale, high deployed/stowed volume ratio), but design optimality and limitations relative to mission requirements are not currently known. In 2001 IRR research produced a significant body of analysis, design and optimization studies.

Carnegie Mellon's contributions in 2002 included the development of analytical models and simulations for the configuration design of IRRs, and extensive configuration trade-off studies. Exploiting various theories of soil mechanics and modern mechanics of soil/vehicle interaction, we developed a framework for characterizing IRR mobility that computes torque, drawbar pull, energy and

power to negotiate a variety of Martian soils. The second component of CMU's work in 2002 was the design and construction of a testing apparatus and sandbox for IRR mobility evaluation.

2 Experimental Characterization of IRR Wheel Mobility

The purpose of this research was to characterize the mobility, obstacle negotiation capability and endurance of a self-propelled IRR wheel in a cohesionless soil medium similar to Martian drift material. We performed a series of experimental studies that quantified the IRR wheel's performance in terms of *rolling resistance, drawbar pull, drive torque, and drive power and energy* to complete a course of action as a function of key variables such as *tire inflation pressure, wheel loading, traveling speed and tire tread design*.

An IRR testbed was developed that consists of an inflatable wheel carried on a support structure capable of carrying the wheel and axle assembly across a test surface in a straight line. The test surface consists of a 10 m x 2 m sandbox in which various materials can be placed such as sand, rocks and obstacles. A brushless DC motor drives the wheel along with motion control hardware and various sensors placed on the testbed.

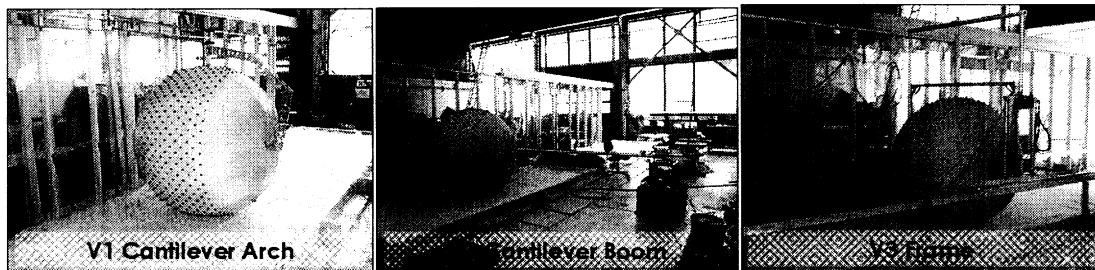


Figure 2: Evolution of the IRR wheel testbed.

Three testbed layouts were implemented (see Figure 2). The first version was designed to integrate with additional actuators that would mimic a steering system and drive motors from additional wheels. However, the cantilever arch design suffered from internal stresses that made measuring wheel mobility difficult. Furthermore, variable loading of the wheel was not straightforward, since additional weight would be unevenly distributed towards the arch attachment.

A cantilever boom design was then implemented to reduce frictional losses in the testbed structure. An additional benefit was that the force of weight on the wheel could be reduced by adding weight to the opposite end of the boom. While the simple design overcame some problems seen with the arch, loading the wheel was still problematic. Again, the weight was unevenly distributed towards the boom side of the wheel. Furthermore, because the wheel traced out an arc around the boom rather than a straight line, the testbed measured steering forces not associated with inherent wheel mobility.

The final testbed design involves a pivoted frame structure around the wheel. Both ends of the wheel axle are attached to the frame (see Figure 3). The frame

allows significant vertical motion of the wheel as it climbs over obstacles, and rides on guide rails to allow motion back and forth in the sandbox. Weights can be attached to the frame and aligned so that the force of weight on the wheel is evenly distributed on both axle attachment points. A motion controller, motor amplifier and other electronics are also mounted on the frame. A minimal amount of cabling provides power to the testbed and links it with a control station nearby.

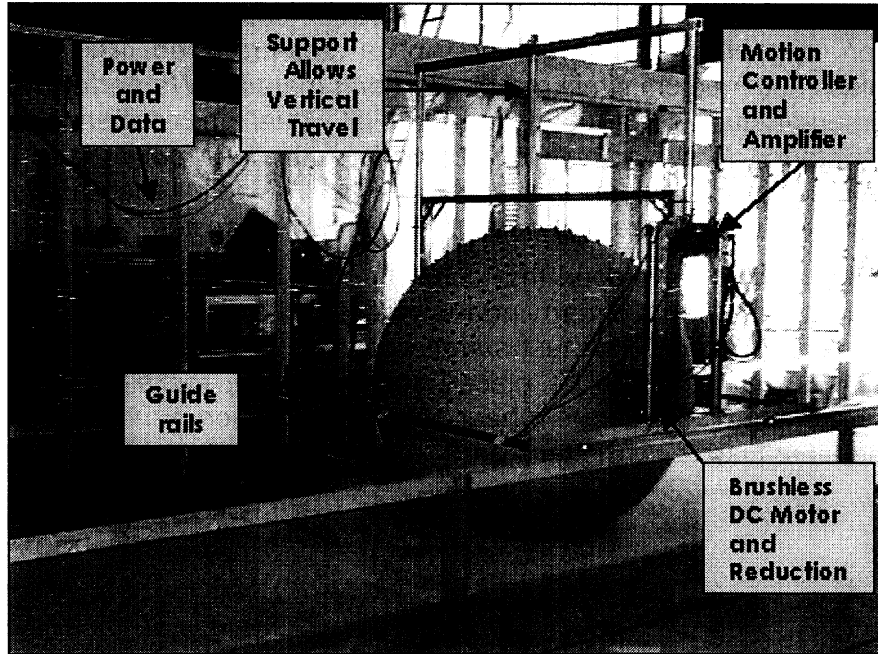


Figure 3: The final testbed layout consists of a frame around the wheel.

The final testbed has been instrumented with load cell and pressure transducers to measure external loading and tire inflation, respectively. Measurements of the drive motor's current combined with measurements of the wheel's rolling radius will be combined to compute drive torque and power. Finally, tire sinkage and contact patch will be measured both during static tests (lower tire into sand) and locomotion tests (average readings after one pass through undisturbed material).

Wheel torque is generated with brushless motor (Hathaway Emoteq Quantum QB01703-C04-HEPI) coupled to the axle via a 3:1 gearbox and a harmonic drive with a ratio of 100:1, resulting in an overall gear ratio of 300:1. The motor is driven by a brushless amplifier (Advanced Motion Controls BD15A8B) and a 300-watt, 48 VDC power supply. A motion controller (J R Kerr Automation PIC-Servo CMC) accepts commands from a RS-232 serial bus and drives the amplifier with PWM output. Encoder signals from the motor provide feedback for the system. A load cell (Transducer Technologies MLP-25 load cell and TM-1 amplifier conditioner) is placed in the support structure to measure the load of the wheel on the test surface. A pressure sensor (SenSyn ASCX05DN) attached to the wheel inflation fitting measures the pressure from 0 to 1 psi within the wheel.

The inflatable wheel testbed was designed to support straightforward execution of experiments and measurement of all necessary variables. The testbed electronic components are organized as shown in Figure 4.

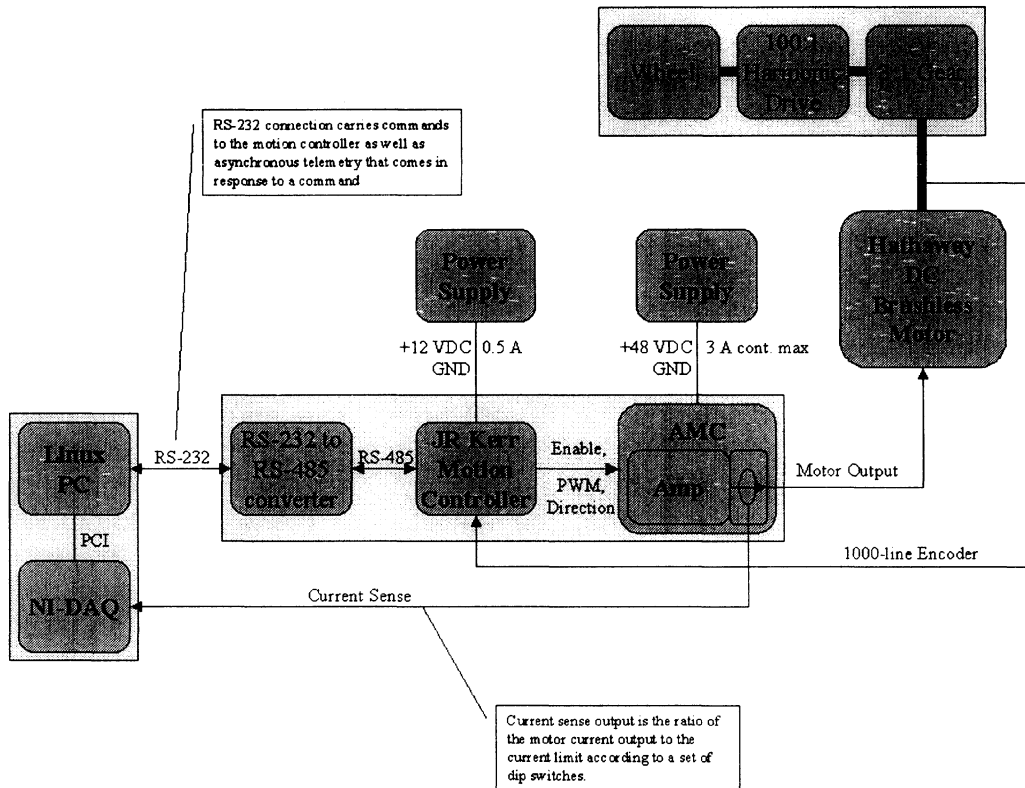


Figure 4: Schematic of IRR testbed electronics.

The testbed allows the control of *wheel angular velocity* (rad/s) and *acceleration* (rad/s^2), which is accomplished through velocity control of the drive motor. These settings, coupled with adjustable wheel weighting and placement of obstacles in the sandbox, provide the experimental configuration. Users specify velocity and acceleration commands on a control station PC through a simple, Linux-based graphical user interface. The GUI sends these commands via TCP/IP to a testbed server process, which in turn communicates via RS-232 to a JR Kerr PIC-Servo motion controller. The motion controller maintains the desired velocity using a PID control loop with feedback from a 1000-line encoder.

The GUI supports two usage modes. First, users can simply command a given velocity and acceleration, press “start” when ready and “stop” when the test is complete. While useful for short tests, this mode is inefficient during extended testing. Therefore a second mode allows users to specify a potentially large set of timed moves, which the GUI executes in order. Limit switches mounted to the rails enable the control station software to automatically stop the wheel if necessary. However hardware stops are also important, as the GUI process (especially those running on standard Linux kernels) can be swapped out for

unpredictable periods of time, suffer network communication delays, or simply crash unexpectedly. Hard stops are therefore also mounted to the rails. If the track runs up against these stops, the motion controller will eventually fault and stop the wheel.

Many variables can be logged during an experiment. Users simply select a log file name, and the GUI proceeds to create or append a log. A server process collects data from several sources at approximately 10 Hz (not real-time), which are then organized by the GUI into a time-stamped, Matlab-compatible log file.

The motion controller itself provides commanded and actual wheel angular velocity and acceleration. Actual velocity and acceleration values are based on differencing encoder feedback. The second measurement device is a National Instruments DAQ card, which is attached to the PCI bus of the Linux PC running the testbed server process. The DAQ card has eight differential analog inputs with 12-bit resolution and sampling times far faster than needed for our application. The testbed server software configures these inputs to range from -5 V to $+5$ V. The DAQ card measures two values. One analog input is connected to the current monitor of the AMC brushless DC motor amplifier. This sensed value represents the output current from the amplifier to the wheel motor. When calibrated, it is able to measure motor output torque. Although the current monitor's accuracy is limited to 10%, the high sampling frequency should provide an accurate sense of mean torque. The 10% inaccuracies become an issue in transitional cases such as obstacle climbing. Another analog input is connected to either a differential pressure sensor or a load cell.

Wheel loading is another important controlled variable in these tests. The cumulative weight of the wheel, axle and frame was measured by driving the wheel onto a digital scale and recording manually the result. The digital scale was accurate to 0.01 kg.

The testbed has also tested two types of tires: one with treads and one without treads. The tire is changed as follows. First, the inner tube is deflated. Next the axle is disconnected from the testbed frame and removed from the tire. The axle is then inserted into the new tire and attached to the testbed frame. The inner tube is then re-inflated.

3 Experimental Characterization of Mobility

3.1 Contact Patch Measurement

Tests of the wheel's static mobility characteristics were carried out first. These included lowering the treaded tire into the sandbox and measuring the wheel loading, its contact patch, its sinkage and the inner tube inflation pressure. Using a digital scale, we found the treaded wheel mass was about 7.5 kg. At this loading, the contact patch was a circle approximately 1300 cm^2 in area (see Figure 5). On average, the tire sank only a few millimeters into the sand. The inflation pressure at this loading was approximately 0.09 psi.

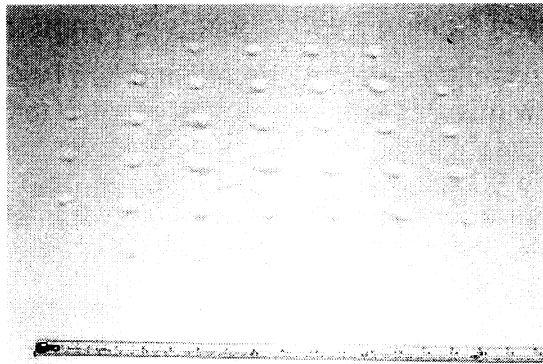


Figure 5: Contact patch of treaded tire in sandbox.

If the wheel loading, soil material (geophysical properties), and contact patch are known, one can use compute the maximum forward thrust (traction) that the wheel /soil system can develop. The developed thrust is determined from the fundamental stress/strain relationship that also accounts for the soil's internal friction and cohesion.

3.2 Flat Terrain Driving

Several tests were performed to understand the interaction between the wheel, with both types of tire, and the cohesionless Mars-analogous soil (see Figure 6). For example, the following figure shows one such test, which involves driving the tire without treads over the testbed. All tests involved the most current testbed implementation.



Figure 6: Smooth tire driving in fine-grained sand.

3.2.1 Coefficient of Rolling Resistance as a Function of Tire Design

Flat terrain tests are useful to measure the effect of tire tread on the coefficient of rolling resistance. Towards this end, we carried out two tests identical except for the tire used. Both tests involved driving the wheel over the flat sandbox with an angular wheel velocity 0.13 rad/s and acceleration of 0.50 rad/s². In both cases, the mass of the wheel was approximately 15.2 kg. The wheel radius along the compressed axis was about 70 cm. The coefficient of rolling resistance was calculated for each sample with the following formula:

$$C_{RR} = T i gear_ratio / F_w / r$$

Where C_{RR} is the coefficient of rolling resistance, T is the drive motor's torque constant in Nm/A, i is the current to the drive motor, $gear_ratio$ is the gear ratio between motor and wheel, F_w is the weight of the wheel in N and r is the radius of the wheels' compressed axis in meters.

Figure 7 summarizes the results of these tests. In this figure we see a representative portion of each test. We see that the coefficient of rolling resistance between both tires and the soil is between 0.10 and 0.15. Over these tests, the smooth tire sees a mean rolling resistance coefficient of 0.13 and the treaded tire sees a slightly lower rolling resistance coefficient of 0.11. Note that in both cases, the rolling resistance increases over time as the wheel traverses the testbed. We postulate on the phenomenon in the next section.

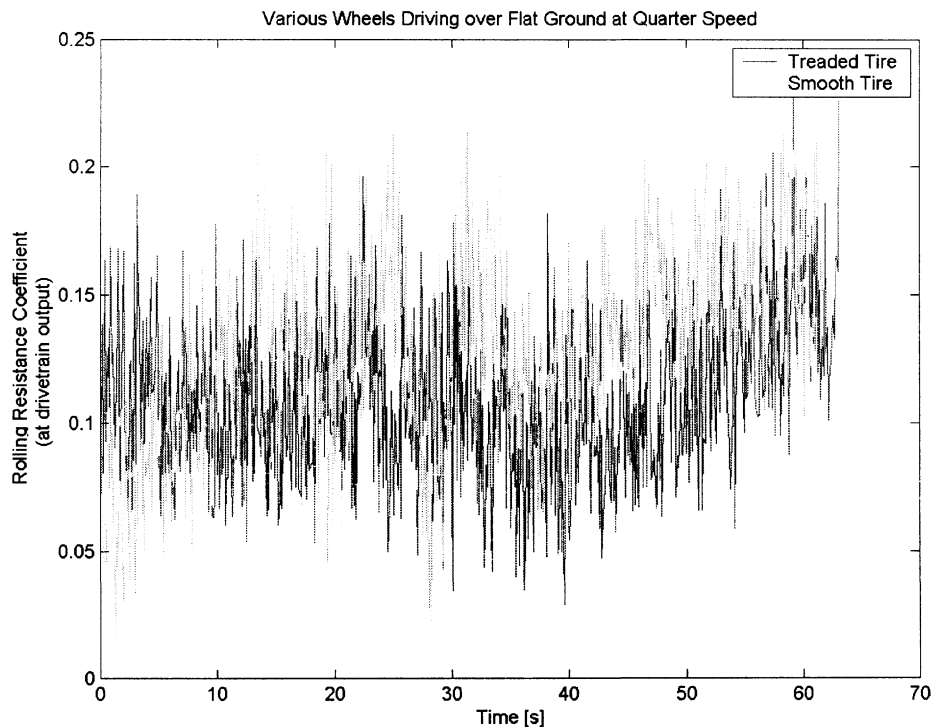


Figure 7: Rolling resistance of the treaded tire is roughly the same as that of the smooth tire (tests A1 and D2).

3.2.2 Effect of Wheel Deformation on Rolling Resistance

As the wheel drives ahead, the current to the motor, and therefore the power consumed, increases. This consistently occurs as the wheel drives in either direction, so the effect cannot be due to a sloped testbed track. Simplistically, a sloped track would result in a trend similar to that shown in the left half of Figure 8. However, we observe trends similar to those shown in the right half of Figure 8. An explanation to this phenomenon probably lies in the fact that the tire is very compliant. As the tire tries to overcome ground resistance force it deforms up to point at which it has gained enough structural rigidity to transmit the necessary torque to overcome the ground resistance and to produce forward motion. Moving forward mitigates the radial deformation of the tire which in turn causes the tire to demand more torque to overcome the resistive ground forces.

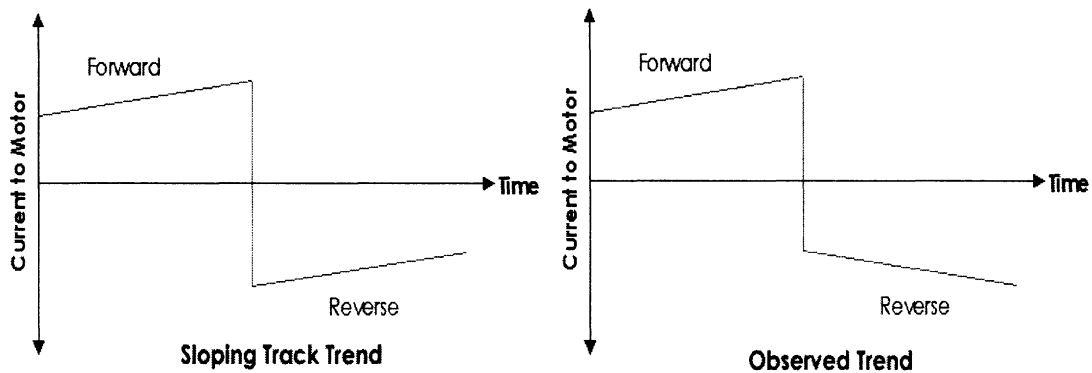


Figure 8: The motor current trend expected from a sloped track (left). Right: the motor current trend observed in flat terrain driving (right).

An example of this effect is shown in Figure 9. Here we plot the motor current of the treaded tire driving over the flat terrain of the sandbox at an angular wheel velocity of 0.13 rad/s, an angular wheel acceleration of 0.50 rad/s² and loaded with 15.15 kg of mass. The radius along the wheel's compressed axis was approximately 71 cm. The cyan data points depict samples taken while driving forward and the pink points depict samples taken while driving in reverse. In both cases, the first several samples in either direction were removed to isolate the steady-state effect. A logarithmic fit is shown for each direction. The logarithm coefficients of both fits are approximately the same, on the order of 4 Nm/s. The torque calculations are accurate to about 7%, limited by the accuracy of our current sensors. See Appendix B for torque calibration data.

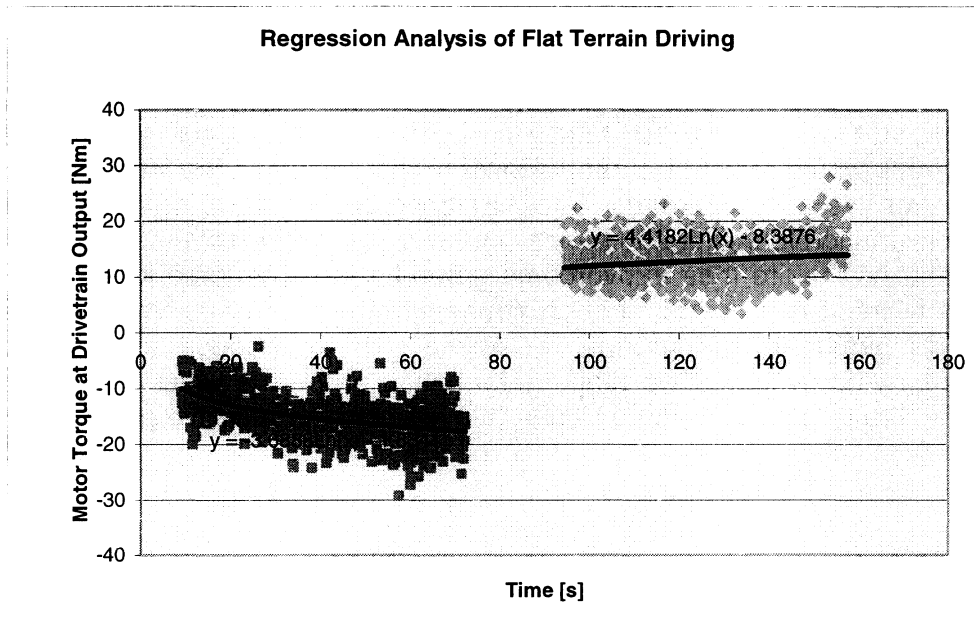


Figure 9: As the wheel drives in either direction, the motor draws more current, perhaps because power is consumed in deforming the wheel itself (test A1).

3.2.3 Coefficient of Rolling Resistance as a Function of Wheel Loading

We also attempted to find the relationship between wheel loading and rolling resistance. The first tests accomplished this for the smooth tire. In two tests the smooth tire was driven with an angular wheel velocity of 0.13 rad/s and an angular wheel acceleration of 0.50 rad/s². Both drove over flat terrain. The two tests differed as shown in Table 1.

Test	Wheel Mass	Wheel Radius, Compressed Axis
D2	15.2 kg	70 cm
D5	20.1 kg	68 cm

Table 1: Comparison of smooth wheel loading tests

The computed coefficient of rolling resistance for those tests is summarized in Figure 10. We see that the results are similar, with average rolling resistance coefficients of between 0.08 and 0.17.

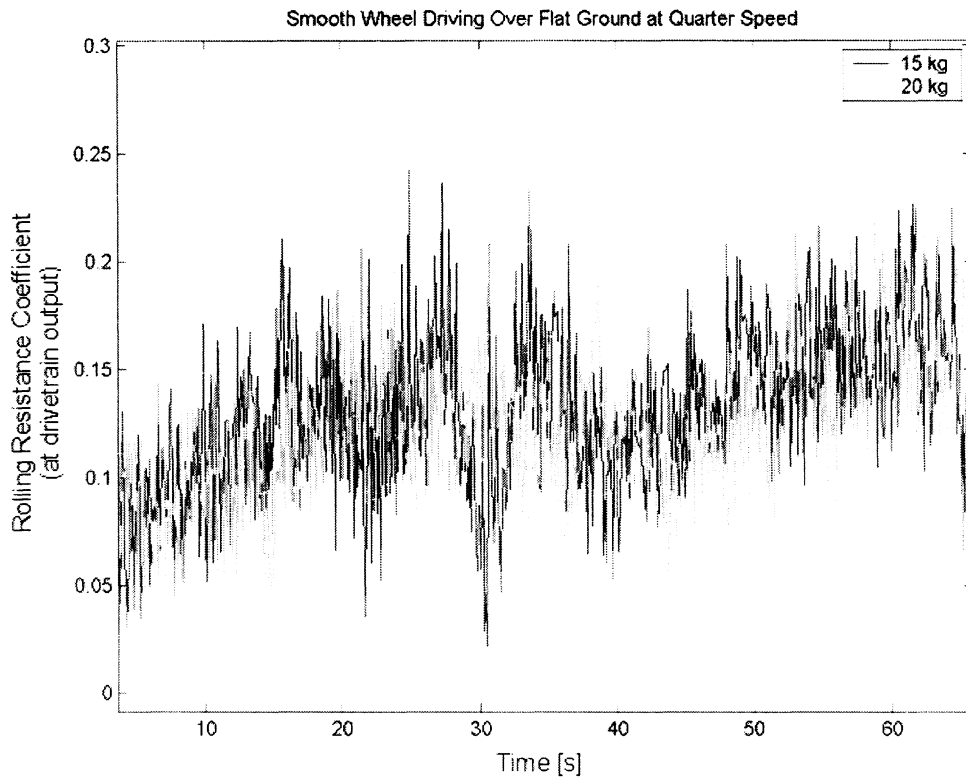


Figure 10: Coefficient of rolling resistance does not change significantly with increased wheel loading (tests D2 and D5).

3.3 Conclusions

The conclusions of our mobility experiments are summarized in Table 2.

Measurement	Result	Significance
Wheel contact patch size	1300 cm ²	Helps predict maximum traction
Wheel sinkage	~ 3 mm	Predicts soil resistance
Locomotion power on flat terrain	Increases asymptotically during run	Indicates how tire deforms and gains structural rigidity
Coefficient of rolling resistance on cohesionless sand	0.11 – 0.13	Coefficient remained fairly constant across tire designs and wheel loadings

Table 2: Outcomes of mobility experiments

4 Experimental Characterization of Obstacle Climbing

4.1 Discrete Obstacle Negotiation

Several tests were performed that tested the wheel's ability to drive over orthogonal, or discrete, obstacles. We used 61 cm x 61 cm x 20 cm wooden blocks to construct obstacles of various sizes (see Figure 11).

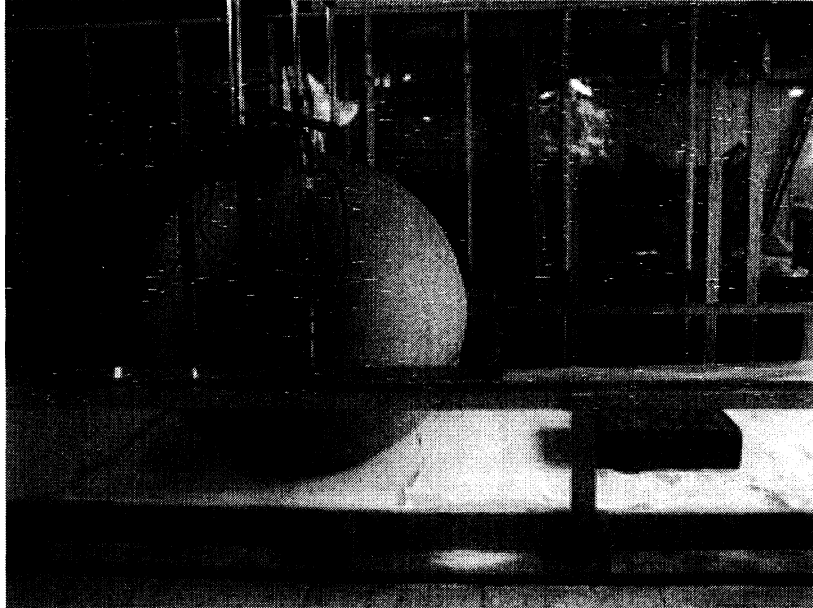


Figure 11: Discrete obstacle negotiation tests on single or stacked orthogonal blocks.

4.1.1 Effect of Wheel Loading on Obstacle Negotiation

The first set of tests with the smooth tire involved driving over a 20-cm obstacle at an angular wheel velocity of 0.13 rad/s and an angular wheel acceleration of 0.50 rad/s². One wheel had a mass of 14.3 kg; the other had a mass of 19.9 kg. Figure 12 shows the interesting results. As the wheels climb the front face of the obstacle (marked with an "A"), the lighter wheel experiences a higher maximum obstacle resistance (1.01) than does the heavier wheel (0.82). This could be because the heavier wheel deforms more over the leading edge of the block. In several cases, if the wheel deforms around the front face of an obstacle, it has better climbing ability.

The part of Figure 12 marked "B" depicts the wheels climbing down the far edge of the obstacle. In this case the motor's current draw (and therefore calculated obstacle resistance coefficient) is negative as the motion controller overcomes the tendency of gravity to back drive the motor. The values here actually represent tractive effort, not obstacle resistance. This should be noted in all subsequent obstacle-climbing tests.

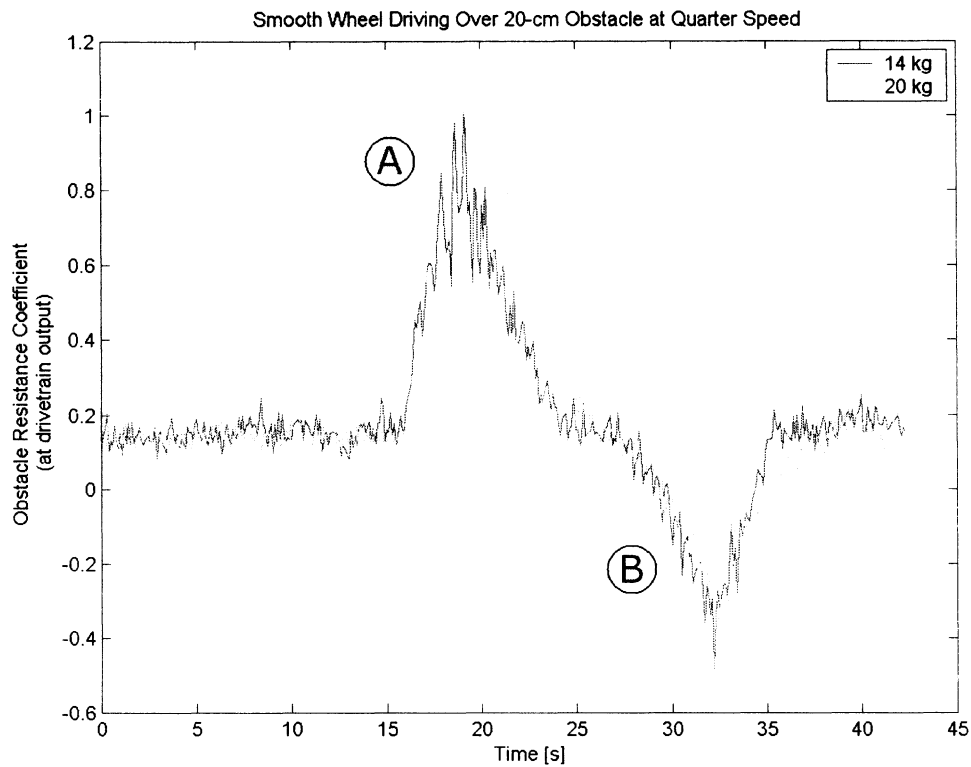


Figure 12: The obstacle resistance coefficient of a smooth wheel with different wheel loadings (tests C1 and F1).

4.1.2 Effect of Tire Design on Obstacle Negotiation

Figure 13 depicts the two tires climbing over a 20-cm obstacle. Both wheels were traveling at 0.13 rad/s with an acceleration of 0.50 rad/s². The mass of the treaded tire was 15.0 kg and the mass of the smooth tire was 14.3 kg. Both had compressed wheel radii of about 70 cm. While climbing up the face of the obstacle, the treaded tire faced less obstacle resistance than the smooth tire. The maximum obstacle resistance coefficient of the treaded tire was 0.88 while the smooth tire's maximum was 1.01. This change in resistance cannot be explained by the 0.7 kg wheel mass difference. Therefore the change quantifies the obstacle climbing benefits provided by the treaded tire.

When climbing down the far edge of the obstacle, neither tire exhibited superior performance. Only the motor torque and wheel mass play a role in climbing down the obstacle.

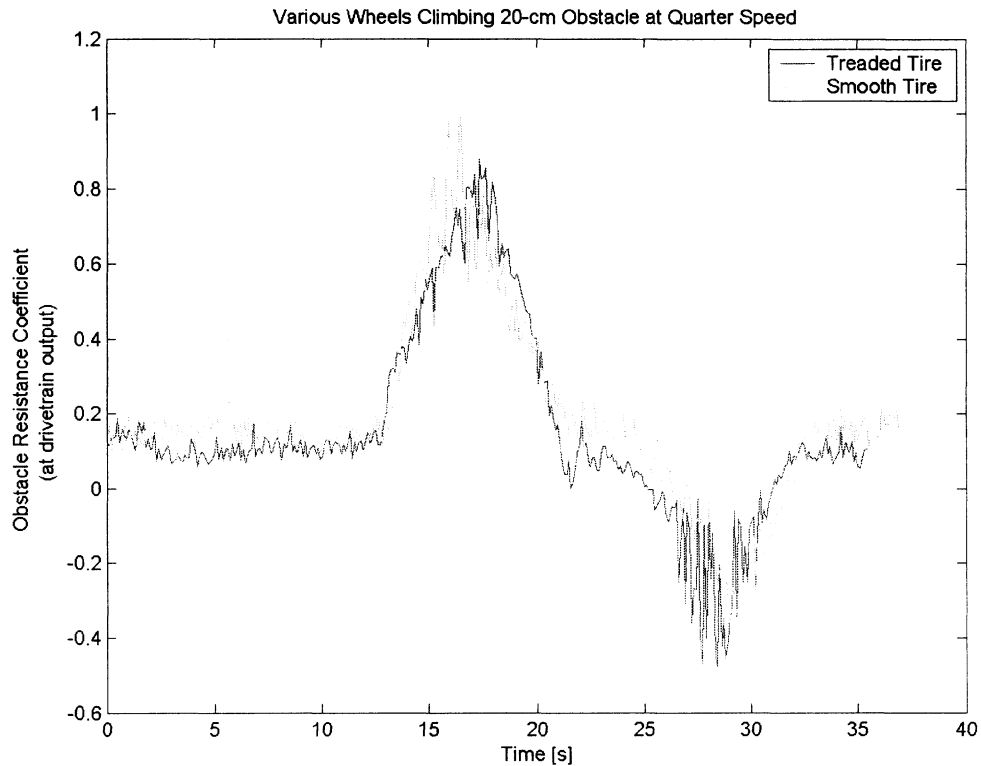


Figure 13: Climbing a 20-cm obstacle with smooth and treaded wheels (tests G2 and C1).

The obstacle-climbing difficulties of a smooth tire are further shown in Figure 14. Here we see the smooth tire attempting unsuccessfully to climb a 40-cm discrete obstacle. About 29 seconds into the test, the wheel meets the front face of the obstacle and begins climbing it. At about 31 seconds, the wheel has not yet climbed the obstacle and begins to slip. This continues for another 7 seconds, at which time the test was cancelled because the wheel could not finish the climb. This test was repeated with similar results. However, Figure 15 in the next section shows that the treaded tire could reliably climb a 40-cm obstacle.

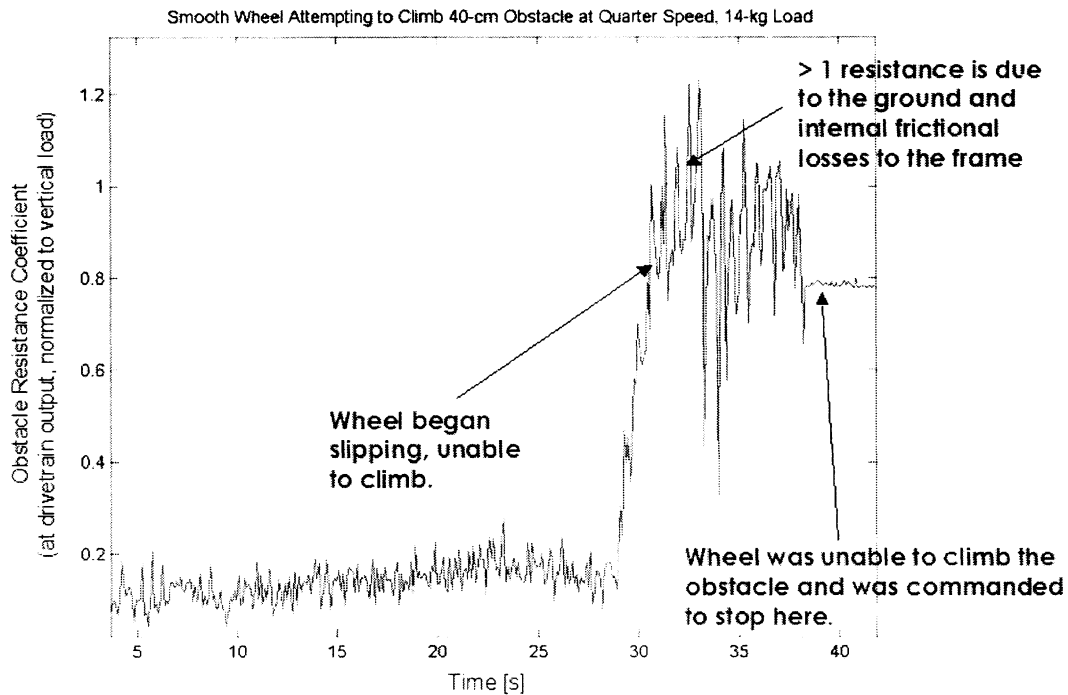


Figure 14: Coefficient of obstacle resistance seen as smooth wheel tried to climb a 40 cm obstacle (test C3).

4.1.3 Effect of Obstacle Height on Obstacle Negotiation

Figure 15 shows the relationship between obstacle height and obstacle resistance coefficient. Both tests involved driving the treaded wheel at 0.13 rad/s velocity and 0.50 rad/s² acceleration towards the obstacle. The blue plot represents the wheel driving over a 40-cm obstacle (two wooden blocks), while the green plot represents the wheel driving over a 20-cm obstacle (one wooden block).

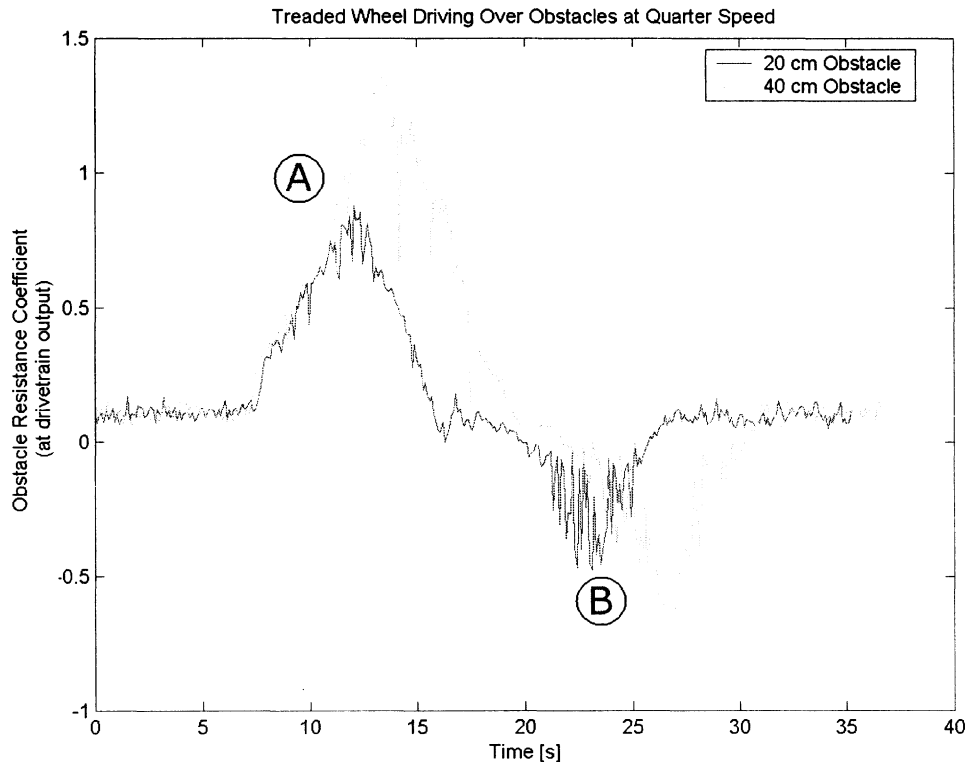


Figure 15: Surmounting obstacles of different heights (tests G2 and G3).

At the outset of both tests, the wheel began driving over the flat sand leading up to the obstacle. As we would expect, both plots are similar in this region. The plots then peak as the wheel pushes into the obstacle. If we look at the apex of these peaks (marked with an “A”) we see that the obstacle resistance reaches nearly 1.5 surmounting the 40-cm obstacle and nearly 1.0 surmounting the 20-cm obstacle. Resistance coefficients larger than 1.0 are due to the ground and frictional losses internal to the frame. Note that the 40 cm obstacle took longer to surmount because the wheel had to slowly pull itself up the obstacle face. The tire’s studs and ability to deform easily helped the wheel drive over the higher obstacle. Further tests will better explore the limits of what size obstacles can be surmounted. A third region of the figure (marked “B”) shows the wheel scaling down the far face of the obstacle. Again, we see that more current (and therefore power) is required to control the motor as it drives down the higher obstacle.

4.2 Complex Obstacle Negotiation

We performed further tests that involved two wooden block obstacles side by side, so that the wheel would climb up one, travel on top of the two blocks and then climb back down. The treaded wheel was used with a 14.98 kg loading and driven at 0.13 rad/s velocity, 0.50 rad/s² acceleration. The obstacle resistance coefficient is plotted in Figure 16.

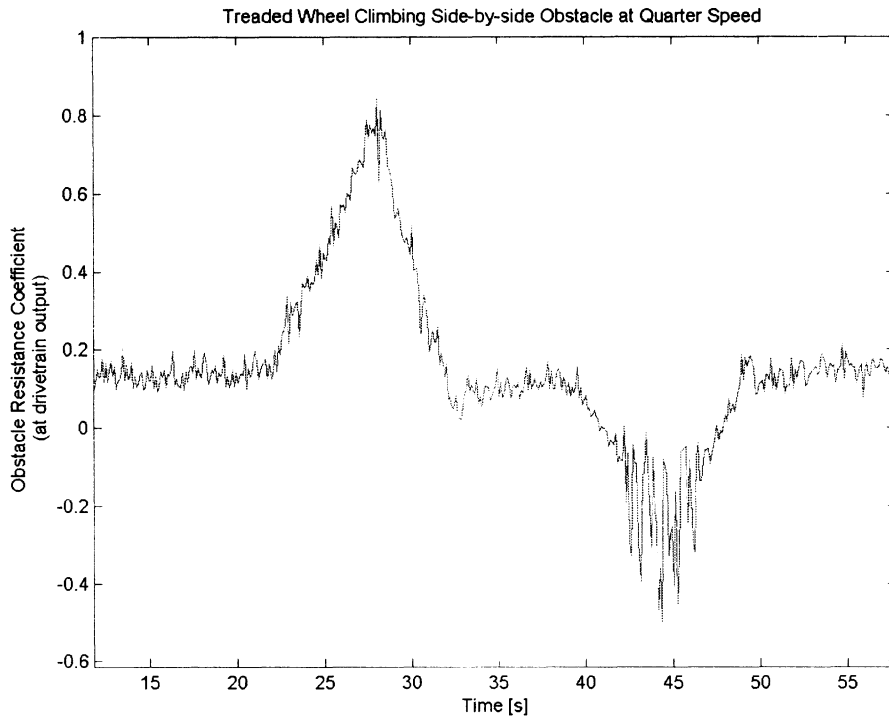


Figure 16: Surmounting “side-by-side” 20 cm obstacle (test H2).

These tests give an idea of how quickly the motor’s current draw rises and falls as the wheel climbs. Climbing up the front face takes approximately 5 seconds. In another 5 seconds the wheel has finished climbing and the motor current draw decreases back to a nominal flat driving level. Understanding the behavior as the wheel climbs down the obstacle is more difficult. An initial analysis shows that it takes approximately 9 seconds for the wheel to reach the threshold, climb down and return to nominal flat driving power levels.

A second complex obstacle was a staggered set of three blocks with a maximum height of 40 cm, as shown in Figure 17.



Figure 17: Three blocks staggered together to create a 40-cm obstacle.

Figure 18 shows the results of the smooth tire climbing over this obstacle with a loading of 14.33 kg, a commanded angular velocity of 0.13 rad/s and acceleration of 0.50 rad/s². The staggered shape of the obstacle enables the smooth wheel to surmount it, unlike the discrete 40-cm obstacle.

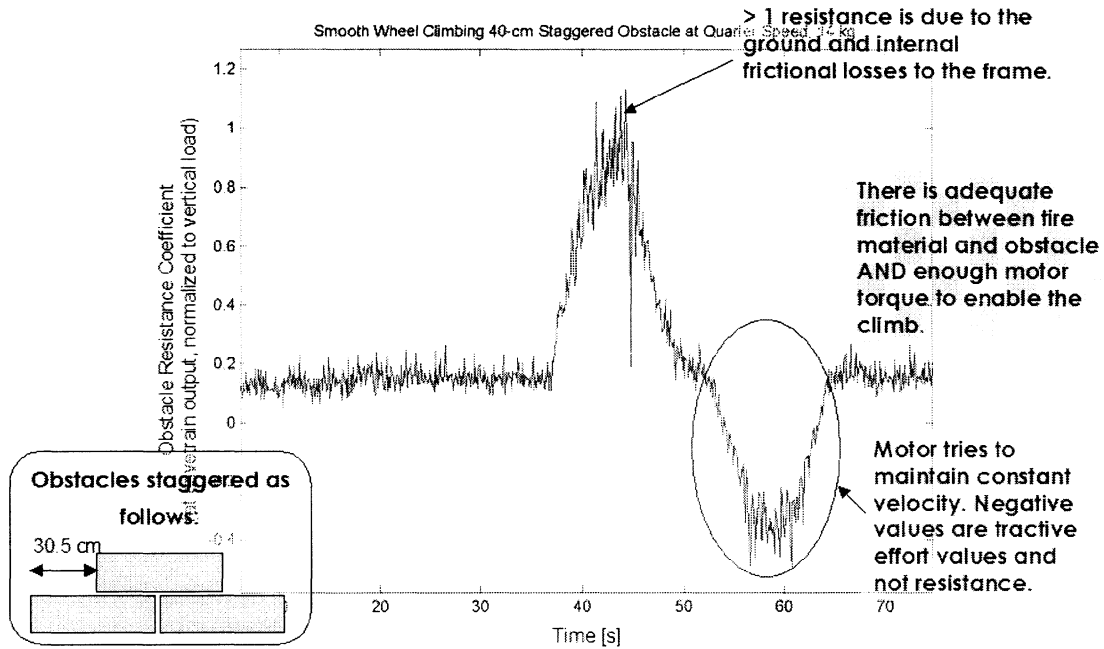


Figure 18: Coefficient of obstacle resistance seen as smooth wheel climbed a staggered 40 cm obstacle (test C5).

4.3 Conclusions

The conclusions of our obstacle climbing experiments are summarized in Table 3.

Measurement	Result	Significance
Obstacle resistance and wheel loading	Heavier wheel experienced less resistance	Wheel deformation plays a significant role in obstacle climbing
Obstacle resistance and tire design	Treaded tire experienced 13% lower resistance Smooth tire could not climb 40-cm obstacle	Treaded tire exhibits superior obstacle-climbing performance
Time to climb obstacle	Wheel traveling at 0.13 rad/s climbed 20-cm obstacle in 10 seconds	Explains relationship between angular wheel velocity and ground speed for a deformable wheel

Table 3: Outcomes of obstacle climbing experiments

5 Drawbar Pull

The maximum drawbar pull capacity of the wheel was determined by measuring the maximum “trailer” force the wheel sustains at reasonable slippage (ideal value of 20%). Figure 19 describes the set up. The wheel was driven while its frame was attached to a fixed surface via a horizontal steel cable. Mounted inline with the cable, a load cell measured the horizontal drawbar pull force as the wheel attempted to propel forward. We characterized the drawbar pull capacity of the tire by plotting the drawbar pull force against tire slippage.

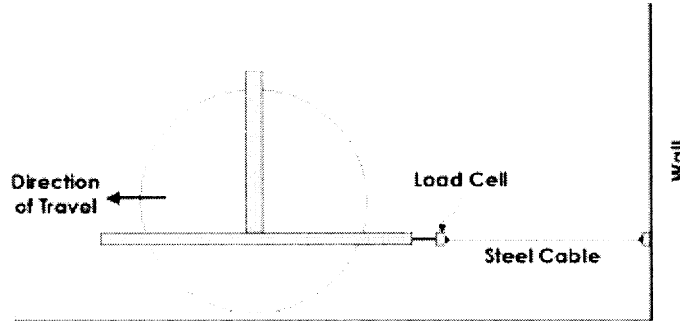


Figure 19: Drawbar pull test set-up

It is worth noting that the arc tangent of the ratio of drawbar pull to wheel loading is approximately equal to maximum gradeability of a IRR could achieve just before the soil that covers the slope fails. This is a particularly useful result because it provides an empirical way of estimating the limit of gradeability independently of the vehicle design and location of the center of gravity or torque / power capacity of its propulsion motors.

The difference between the measured drawbar pull and computed thrust equals the motion (rolling) resistance at the wheel. This is an alternative way to estimate rolling resistance and the associated coefficient of rolling resistance in addition to the method pursued in the flat terrain and obstacle negotiation tests.

Each drawbar pull test consists of five operating regions. In region “A”, the wheel driving away from the wall, extending the steel cable but still driving normally. In region “B” the cable tension rapidly increases and so the tire begins to deform. Deformation continues until region “C”, where the wheel begins slipping and the cable remains taught. This continues until region “D” when the wheel is commanded to stop. The cable then begins to slack in region “E” and the wheel drives back towards the wall.

Figure 20 depicts two of six the smooth tire drawbar pull tests. With a 15-kg wheel loading (left figure), the wheel exerts over 90 N of force on the steel cable. Maximum force on each test was 94 N, 96 N and 96 N. Increasing the wheel loading to 20 kg (right figure) enables the wheel to exert a maximum 138 N of force on each of three tests.

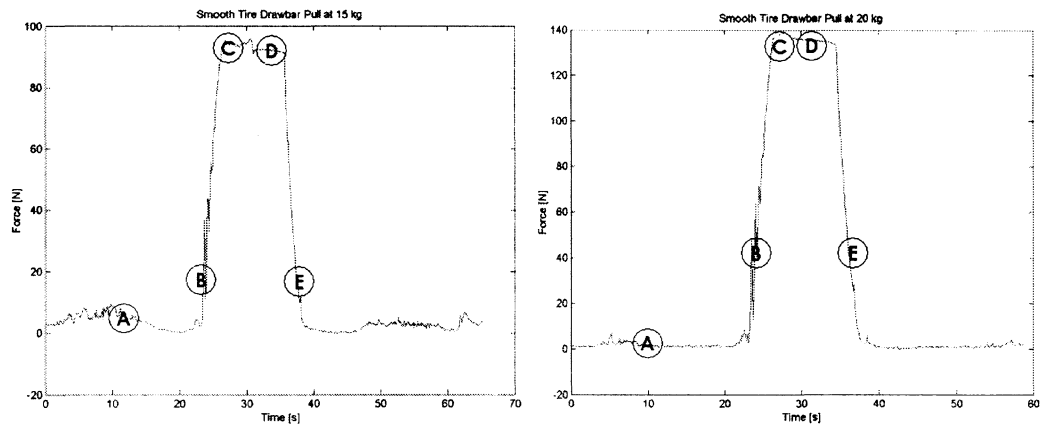


Figure 20: Drawbar pull tests with smooth tire at 15-kg (left) and 20-kg (right) wheel loading.

Figure 21 depicts all three tests with the treaded tire loaded at 15 kg. Maximum force on each test was 138 N, 136 N and 138 N. Sensor noise was seen on these tests, particularly in the areas of normal driving (region “A” and after region “E”). Therefore all three tests were shown.

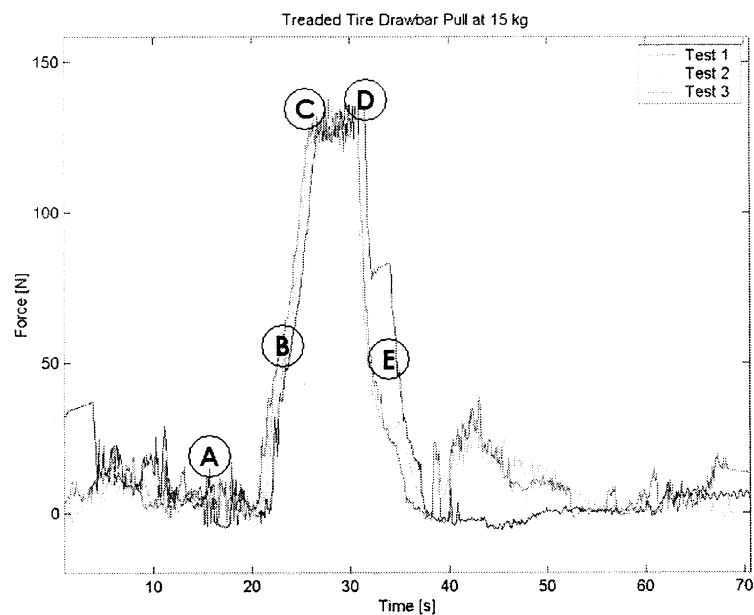


Figure 21: Drawbar pull tests with treaded tire at 15-kg wheel loading.

Drawbar pull results, including maximum gradeability calculations, for each configuration are shown in Table 4. The maximum theoretical climbing angle for the smooth tire is 32 – 35 degrees while the treaded tire should be able to climb a 43-degree angle.

Date	Test #	Tire	Loading [kg]	Loading [kg]	Max Drawbar Pull [N]	Climbability [deg]
19-Sep-02	1	Smooth	15.23	149.25	94	32.20
19-Sep-02	2	Smooth	15.23	149.25	96	32.75
19-Sep-02	3	Smooth	15.23	149.25	96	32.75
24-Sep-02	13	Smooth	20.09	196.88	138	35.03
24-Sep-02	14	Smooth	20.09	196.88	138	35.03
24-Sep-02	15	Smooth	20.09	196.88	138	35.03
03-Feb-03	4	Treaded	14.98	146.80	138	43.23
03-Feb-03	5	Treaded	14.98	146.80	136	42.81
03-Feb-03	6	Treaded	14.98	146.80	138	43.23

Table 4: Wheel climbability results based on drawbar pull data.

6 IRR Endurance Testing

At the conclusion of our testing program we conducted a series of endurance runs during which the tire drove back and forth on the testbed hundreds of times accumulating more than 50 km of distance traveled in sand and nearly 10 km of distance traveled through a rocky course (populated sandbox with abrasive mars-like volcanic rocks). The purpose of the endurance test was twofold: To characterize the wear on the tire material and to assess the overall reliability of self-propelled wheel design. We conducted endurance tests using both the smooth and cleated IRR tires. The smooth tire traveled 50 km in sand and both tires traveled 10 km on rocky terrain. Each wheel was driven at 0.13 rad/s angular velocity and 50 rad/s² angular acceleration and had a loading of approximately 15 kg.

Tens of kilometers of driving through the sandy soil caused no visible wear to the smooth tire (see Figure 22). We examined the tires at about each kilometer of travel for significant wear indicators. Simple visual examinations and examinations under 3x optical magnification revealed no measurable wear.

After a few kilometers of travel the tire would be re-inflated. Tire deflation would occur within the next hour. Because the tire commonly traveled deflated, it left a wide track in the sandbox. The tire track was nearly 1 m in width and consisted of repeating ridges about 5 cm wide and 3 cm high.

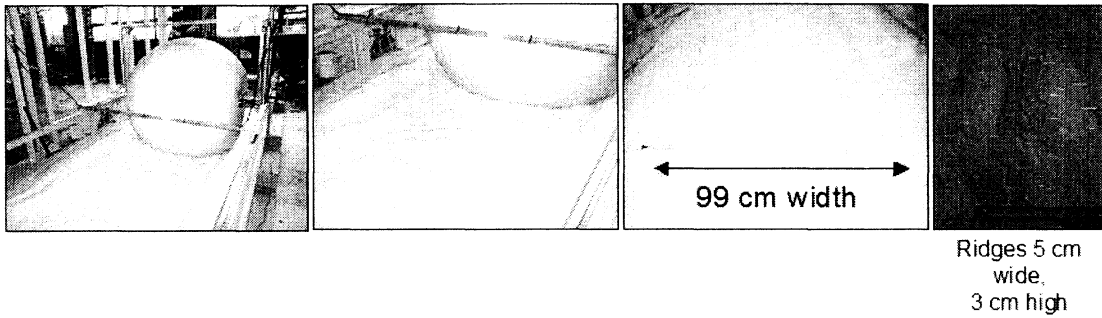


Figure 22: After more than 50 km of travel over sand, the smooth tire had no noticeable wear but left a wide track in the sandbox.

The tires performed differently when subjected to the rock-cluttered testbed (see Figure 23). Wear became evident even from the very first endurance test laps. Rock abrasion produced scratches on and discolorization of the tires. The significant tire surface wear shown in Figure 24 was measured at the conclusion of those endurance runs.

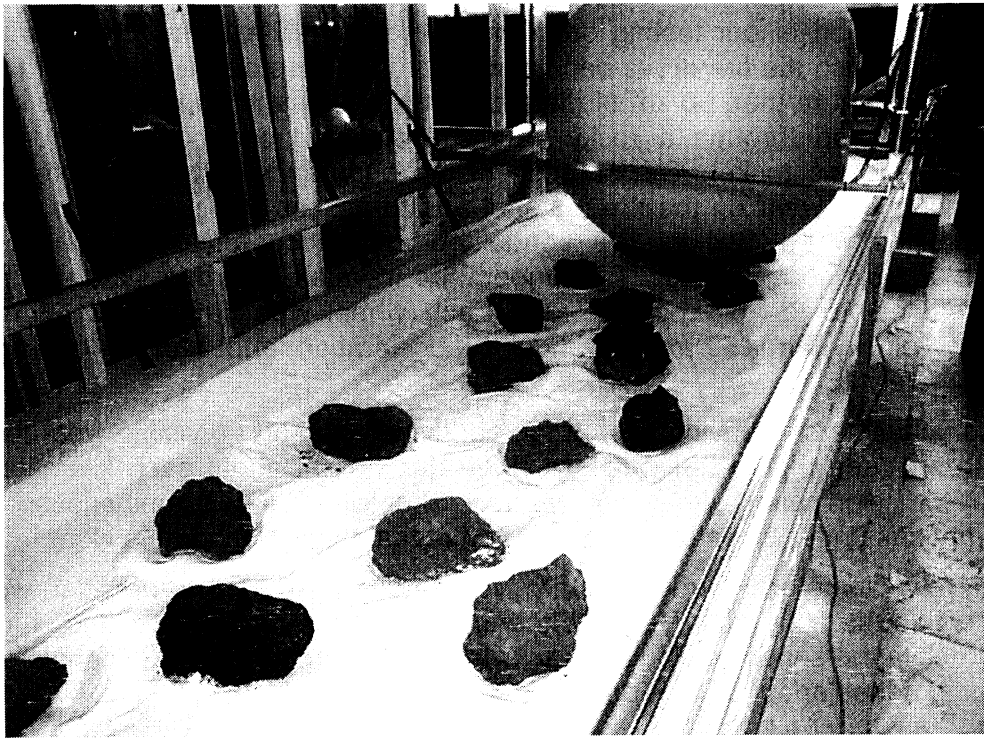


Figure 23: Smooth IRR wheel during rough terrain endurance tests.



Figure 24: Significant tire surface wear due to repetitive traffic over abrasive Mars-like volcanic rocks (Left: Tire driving over rock, Right: Close-up image of the worn tire as indicated by discolorization and scratches).

7 Summary

The main contributions and results of this work have been:

- Experimentally characterized inflatable wheel mobility as a function of tire construction, loading and inflation. Conducted more than 50 experiments in various terrain conditions and geometries, including discrete orthogonal and combined steps, slopes, etc.
- Quantified tire rolling resistance in weak frictional sand, compacted sloped terrain and hard obstacles. Observed typical rolling resistance coefficients of 0.10 – 0.15 in sand. Statistically similar results were obtained for the smooth and treaded tires. The treaded tire had a lower maximum obstacle resistance coefficient (0.8) for a 20-cm step climb than the smooth tire (1.0).
- Quantified drawbar pull capacity and projected vehicle gradeability through traction experiments. Experiments showed significant pull capacity of 70% of wheel loading and slope climbing capability higher than the frictional limit of sand (>35 deg).
- Evaluated limitations of single inflatable wheel performance especially in terms of step climbing at various inflations and loading conditions.
- Characterized wear resistance of the inflatable tire though over 50 km of endurance traverses in a closed test course.

8 Bibliography

- [1] Jones, J., "Inflatable Robotics for Planetary Exploration," Proceedings of the 6th International Symposium on Artificial Intelligence, Robotics, and Automation in Space, I-SAIRAS, Montreal, Canada, June 2001.
- [2] Scott, D., "This Walking Wheel Turns Itself," Popular Science Article, July 1964, pp. 44-46.
- [3] Jones, J., and J. J. Wu, "Inflatable Rovers for Planetary Applications," Proceedings of the SPIE International Symposium on Intelligent Systems and Advanced Manufacturing, September 19-22, Boston, Massachusetts.
- [4] Matijevic, J. R., et. al, "Characterization of the Martian Surface Deposits by the Mars Pathfinder Rover, Sojourner," Science, vol. 278, December 1997, pp. 1765-1767.
- [5] Bernard, D., "Preliminary Look at Hazard Models for Mars Landing," JPL Interoffice Memorandum, IOM3412-00-20, March 2000.
- [6] Bernard, D., and M. Golombek, "Crater and Rock Hazard Modeling for Mars Landing," Proceedings of the AIAA Space 2001 Conference, Albuquerque, NM, August 2001.
- [10] Moore, H., and B. Jakosky, "Viking Landing Sites, Remote-Sensing Observations, and Physical Properties of Martian Soil Materials," Icarus, vol. 81, 1989, pp. 164-184.
- [11] Moore, H., and G. Clow, "A Summary of Viking Sample-Trench Analyses for Angles of Internal Friction and Cohesions," Journal of Geophysical Research, vol. 87, no. B12, November 1982, pp. 10,043-10,050.
- [12] Bekker, M., Theory of Land Locomotion, University of Michigan Press, Ann Arbor, MI, 1956.
- [13] McCarthy, D. F., Essentials of Soil Mechanics and Foundations, Reston Publishing Company, Inc., Reston, VA, 1982.

9 Appendices

Appendix A: Summary of Mobility Experiments Performed

The experimental setups for all mobility and obstacle climbing tests are summarized below. The test IDs below are referenced in figures throughout the text. Note that grey numbers in the “Initial Compressed Radius” column represent measurements estimated based on previous tests.

Test ID	Date	Tire	Velocity [rad/s]	Accel [rad/s ²]	Wheel Mass [kg]	Terrain	Initial Compressed Radius [cm]	Result
A1	29-Jul-02	Treads	0.13	0.5	15.15	Flat	71.1	Success
A2	29-Jul-02	Treads	0.25	0.5	15.15	Flat	71.1	Success
A3	29-Jul-02	Treads	0.37	0.5	15.15	Flat	71.1	Success
A4	29-Jul-02	Treads	0.13	0.5	15.15	1 obs	71.1	Success
A5	29-Jul-02	Treads	0.25	0.5	15.15	1 obs	71.1	Success
B1	22-Aug-02	Treads	0.25	0.5	15.20	Flat	72.4	Success
B2	22-Aug-02	Treads	0.25	0.5	20.50	Flat	71.1	Fail
B3	22-Aug-02	Treads	0.25	0.5	21.41	Flat	71.1	Success
B4	22-Aug-02	Treads	0.25	0.5	21.41	1 obs	71.1	Fail
B5	22-Aug-02	Treads	0.13	0.5	21.41	1 obs	71.1	Fail
B6	22-Aug-02	Treads	0.13	0.5	21.41	1 obs	69.2	Success
B7	22-Aug-02	Treads	0.13	0.5	15.29	1 obs	70.5	Success
C1	17-Sep-02	Smooth	0.13	0.5	14.33	1 obs	70.5	Success
C2	17-Sep-02	Smooth	0.13	0.5	14.33	1 obs	69.9	Success
C3	17-Sep-02	Smooth	0.13	0.5	14.33	2 obs	69.9	Fail
C4	17-Sep-02	Smooth	0.13	0.5	14.33	3 staggered	69.9	Fail
C5	17-Sep-02	Smooth	0.13	0.5	14.33	3 staggered	69.9	Success
C6	17-Sep-02	Smooth	0.13	0.5	14.33	side-by-side	70.5	Success
D1	24-Sep-02	Smooth	0.13	0.5	15.20	Flat	71.4	Fail
D2	24-Sep-02	Smooth	0.13	0.5	15.20	Flat	69.9	Success
D3	24-Sep-02	Smooth	0.25	0.5	14.88	Flat	68.6	Success
D4	24-Sep-02	Smooth	0.37	0.5	14.83	Flat	66.0	Success
D5	24-Sep-02	Smooth	0.13	0.5	20.05	Flat	67.9	Success
D6	24-Sep-02	Smooth	0.25	0.5	20.05	Flat	64.1	Success
D7	24-Sep-02	Smooth	0.25	0.5	20.05	Flat	64.1	Success
D8	24-Sep-02	Smooth	0.37	0.5	20.05	Flat	63.5	Success

E1	26-Sep-02	Smooth	0.25	0.5	19.87	1 obs	68.6	Success
E2	26-Sep-02	Smooth	0.38	0.5	19.87	1 obs	69.2	Success
E3	26-Sep-02	Smooth	0.25	0.5	19.87	3 staggered	68.6	Fail
E4	26-Sep-02	Smooth	0.25	0.5	19.87	3 staggered	68.6	Fail
E5	26-Sep-02	Smooth	0.25	0.5	19.87	3 staggered	66.7	Fail
E6	26-Sep-02	Smooth	0.25	0.5	19.87	3 staggered	66.0	Fail
E7	26-Sep-02	Smooth	0.25	0.5	19.87	3 staggered	65.4	Success
E8	26-Sep-02	Smooth	0.25	0.5	19.87	3 staggered	65.4	Success
E9	26-Sep-02	Smooth	0.25	0.5	19.87	3 staggered	63.5	Success
E10	26-Sep-02	Smooth	0.13	0.5	19.87	3 staggered	61.0	Success
E11	26-Sep-02	Smooth	0.13	0.5	19.87	2 obs	61.6	Fail
E12	26-Sep-02	Smooth	0.13	0.5	19.87	2 obs	59.7	Fail
E13	26-Sep-02	Smooth	0.25	0.5	19.87	2 obs	58.7	Fail
E14	26-Sep-02	Smooth	0.13	0.5	19.87	2 obs	57.8	Fail
F1	30-Sep-02	Smooth	0.13	0.5	19.91	1 obs	67.3	Success
F2	30-Sep-02	Smooth	0.13	0.5	14.24	2 obs	68.6	Success
G2	04-Feb-03	Treads	0.13	0.5	14.98	1 obs	72.4	Success
G3	04-Feb-03	Treads	0.13	0.5	14.98	2 obs	69.9	Success
H1	05-Feb-03	Treads	0.13	0.5	14.98	3 staggered	72.4	Success
H2	05-Feb-03	Treads	0.13	0.5	14.98	side-by-side	67.3	Success
H3	05-Feb-03	Treads	0.25	0.5	14.98	side-by-side	72.4	Success
H4	05-Feb-03	Treads	0.25	0.5	14.98	3 staggered	71.1	Success
H5	05-Feb-03	Treads	0.25	0.5	14.98	2 obs	71.1	Success
H6	05-Feb-03	Treads	0.25	0.5	14.98	1 obs	69.9	Success
H7	05-Feb-03	Treads	0.38	0.5	14.98	1 obs	67.3	Success
H8	05-Feb-03	Treads	0.38	0.5	14.98	2 obs	67.3	Success
H9	05-Feb-03	Treads	0.13	0.5	20.70	2 obs	72.4	Fail
H10	05-Feb-03	Treads	0.13	0.5	20.70	2 obs	72.4	Fail
H11	05-Feb-03	Treads	0.13	0.5	20.70	1 obs	72.4	Success
H12	05-Feb-03	Treads	0.25	0.5	20.70	1 obs	69.9	Success
H13	05-Feb-03	Treads	0.38	0.5	20.70	1 obs	69.9	Success
H14	05-Feb-03	Treads	0.13	0.5	20.70	2 obs	68.6	Fail
H15	05-Feb-03	Treads	0.13	0.5	20.70	2 obs	66.0	Fail
H16	05-Feb-03	Treads	0.13	0.5	20.70	2 obs	62.2	Fail

Appendix B: Torque Calibration Data

The single-wheel testbed does not provide a direct measurement of torque at harmonic drive output. Rather, the motor amplifier in the testbed includes a current sensor that measures current to the wheel motor. Determining the torque applied to the wheel requires therefore requires a conversion factor.

Calibrating for this conversion factor involved an apparatus shown in Figure 25. An arm with attachment points along it was attached to the harmonic drive output. Known weights were attached at these points and the motor was commanded to hold the arm at an angle parallel to the ground. With the mass, distance from the attachment point to the gear and arm angle, the hold torque can be calculated. The amplifier's current sensor output was recorded at 10 Hz for 60 seconds.

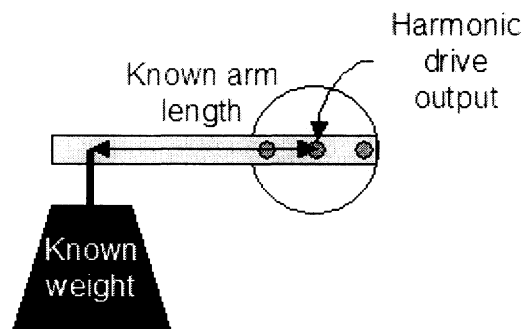


Figure 25: Torque calibration involved measuring a known hold torque at the gearbox output.

Eighteen tests were performed with masses from 10.6 kg to 31.5 kg and arm lengths from 0.1 m to 0.3 m. The average and standard deviation of the torque-current ratio throughout the test are recorded below. The overall conversion factor is simply the average conversion factor for all tests. However, three tests were eliminated from this average because they exhibited unusual oscillations in current, which resulted in a high standard deviation of torque-current ratio. The eliminated tests are shown below in grey.

Date	Test #	Mass [kg]	Length [m]	Arm Angle [deg]	Torque [Nm]	Mean Current [A]	Stdev Current [A]	Conversion [Nm/A]	Fit Torque [Nm]	Fit Error [Nm]	Fit Error [%]
18-Nov	1	10.58	0.20	0.50	20.74	0.53	0.01	38.92	21.25	0.51	2%
18-Nov	2	10.58	0.20	0.80	20.73	0.55	0.05	37.75	21.91	1.18	6%
18-Nov	3	16.04	0.20	1.10	31.43	0.96	0.01	32.91	38.09	6.66	21%
18-Nov	5	31.50	0.20	1.30	61.72	1.67	0.01	36.94	66.65	4.92	8%
18-Nov	6	31.50	0.25	1.50	77.15	1.82	0.02	42.47	72.45	4.70	6%
22-Nov	1	15.82	0.30	1.40	46.50	1.15	0.01	40.35	45.96	0.53	1%
22-Nov	2	15.82	0.25	1.30	38.75	0.95	0.01	40.99	37.71	1.04	3%

22-Nov	3	15.82	0.20	0.70	31.00	0.82	0.01	38.00	32.55	1.54	5%	
22-Nov	4	15.82	0.15	0.80	23.25	0.57	0.01	40.72	22.77	0.48	2%	
22-Nov	5	15.82	0.10	0.40	15.50	0.53	0.03	29.50	20.97	5.46	35%	
22-Nov	6	10.55	0.10	1.00	10.34	0.38	0.14	27.45	15.02	4.68	45%	
22-Nov	7	10.55	0.15	0.20	15.51	0.44	0.01	35.02	17.66	2.16	14%	
22-Nov	8	10.55	0.20	0.40	20.68	0.48	0.01	42.65	19.34	1.34	6%	
22-Nov	9	10.55	0.25	0.60	25.85	0.61	0.01	42.29	24.38	1.47	6%	
22-Nov	10	10.55	0.30	0.70	31.01	0.74	0.01	42.19	29.32	1.69	5%	
22-Nov	11	31.50	0.10	0.60	30.87	0.73	0.01	42.05	29.28	1.58	5%	
22-Nov	12	31.50	0.15	0.80	46.30	1.08	0.02	42.92	43.03	3.27	7%	
					MIN:	15.51			MEAN:	39.89		
					MAX:	77.15			STDEV:	3.12		
									MEAN:	7%		
									STDEV:	5%		

Figure 26 shows how well the 39.89 Nm/A conversion factor fits the test data.

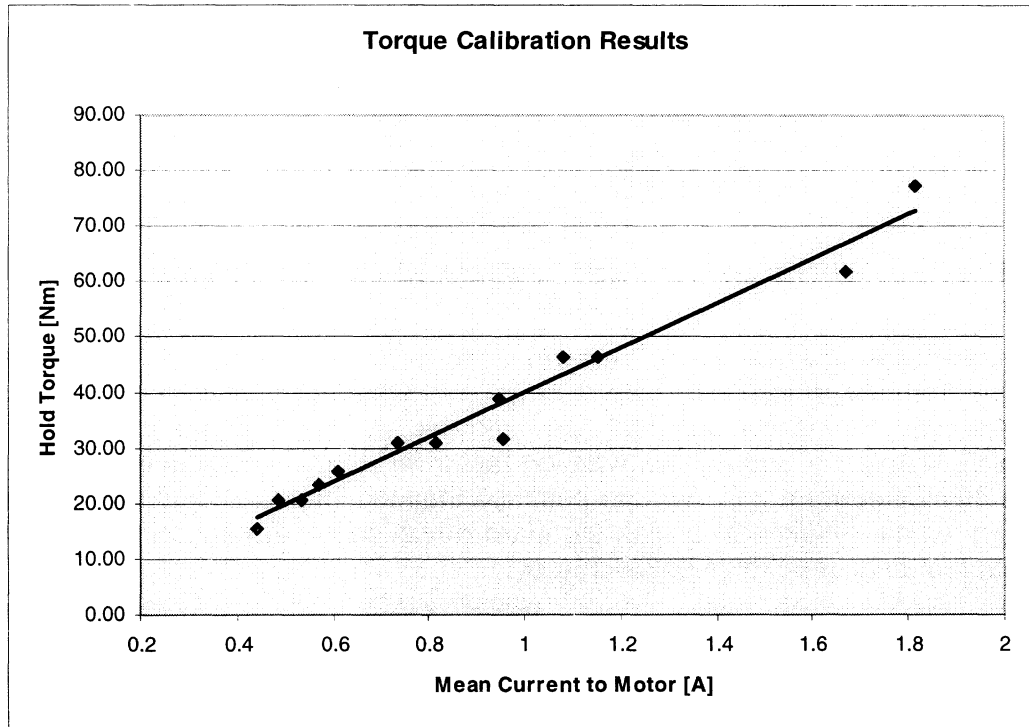


Figure 26: The calibrated torque-current ratio (black line) plotted against test data (blue dots).